

CFRP TORSION BAR: LOAD INTRODUCTION PROBLEM

Gerald R. Kress, Paolo A. Ermanni
Centre of Structure Technologies, ETH Zurich
Leonhardstr. 27, CH-8092 Zurich, Switzerland

Keywords: *Torsion bar, fiber reinforced plastics, FEM, optimization*

Abstract

Torsion bars made from carbon fiber reinforced plastics (CFRP) can be shown, by simplified preliminary stress analysis, to outperform those made from steel. A remaining problem is to introduce the torsion moment into the fiber-wound bar. This work investigates the load introduction problem connected with, and to be solved by, a proposed design and manufacturing principle.

Key words: torsion bar, fiber-reinforced plastics, FEM, optimization

1 Potential of CFRP Torsion Bars

Torsion bars as automotive suspension spring elements have been made quite popular by the mass-production car VW ‘Beetle’ and, far into the 80ties, the sports car Porsche 911. Today the principle is less often found in passenger cars than track vehicles such as tanks.

The performance of springs depends on stiffness and strength properties. The high limit strains and low weight of fiber reinforced plastics (FRP) appear attractive. Consequently, leaf springs are used in trucks and also in the well-known sports car Chevrolet Corvette.

This work investigates the potential of fiber-reinforced plastics for torsion bars. Section 2 presents initial sizing considerations. Section 3 discusses the problem of introducing the torque into the bar and suggests a possible design principle for solving it. From the design principle we derive the design and analysis models explained in Section 4. Section 5 details the automated optimization procedure for sizing and Section 6 presents and discusses the obtained results. The conclusions are found in Section 7.

2 Initial Sizing Considerations

The following sub-sections recall sizing formulae for torsion bars made from isotropic materials. The analysis of a thick-walled tube illuminates the potential and limits of fiber-reinforced plastics.

2.1 Sizing Formulae for Metals Recall

For the sizing of torsion bars with circular cross-section one finds in engineering handbooks [1] the formulae for admissible torque T

$$T = \frac{\pi}{16} d^3 \tau_{adm} \quad (1)$$

where d and τ_{adm} denote the diameter and the admissible shear stress, respectively. The torsion stiffness c is calculated by

$$c = \frac{\pi d^3}{32l} G \quad (2)$$

with length l and shear modulus G . The stiffness c relates torque T and angle φ over the length l :

$$\varphi = \frac{T}{c} \quad (3)$$

It is often desired that torsion springs can withstand a specified torque and allow for high rotation at the same time. Thus, the length-specific internal energy,

$$u = \frac{1}{2} T \varphi = \frac{\pi d^2}{16G} \tau_{adm}^2 \quad (4)$$

is a measure of spring efficiency.

2.2 Composite Torsion Bar Potential

A preliminary investigation compares the potential of carbon-fiber reinforced plastics (CFRP) with that of spring steel. It considers a torsion spring model where Fig. 1 illustrates that a composite body is wound around a steel mandrel. It is modeled as a sequence of cylindrical shells with a $[\pm 45_n]_s$ stacking sequence.

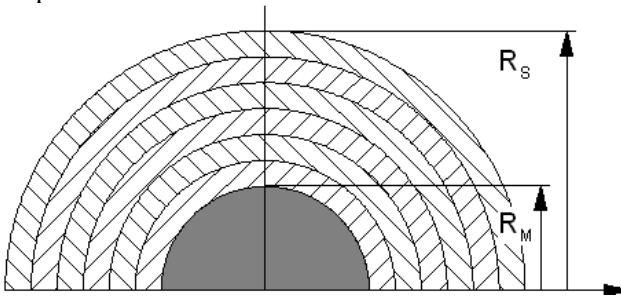


Fig. 1. Composite Spring Wound on Steel Mandrel

The shells, or layers, consist of high-performance CFRP material and we use the properties given in Table 1.

Table 1. Material Properties

		Toolox 44	T-1000 Epoxy
G	[MPa]	80769.00	45337.00
τ_{ult}	[MPa]	693.00	680.00
ρ	[g/cm ³]	7.85	1.60

The shear modulus value assigned to CFRP holds for a $[\pm 45_n]_s$ laminate and it is calculated by the theory of laminate plates [2]. The strength value corresponds with first-ply failure which is matrix cracking. Please note that the strength values of both materials are similar while the composite provides a higher compliance.

The radius R_S of the spring is fixed and that of the mandrel, R_M , varies from zero to R_S , enclosing in the range the pure carbon and pure steel spring designs. The evaluation of the structural behavior of the spring uses a FORTRAN code after an exact theory for thick-walled composite tubes [3]. Fig. 2 presents the graphical results overview output of the program. The radial displacement variations are caused by material anisotropy (upper left). The shear strain increases linearly from the center to the surface while the radial strain oscillates from layer to layer (center left). The shear stress increases more rapidly in the steel core although higher values are reached further out in the CFRP body where the circumferential stresses alternate from layer to layer (bottom left). A similar alternating pattern appears in

the local fiber stress distribution shown in the bottom center plot. Although the fiber stresses are much smaller, the probability of matrix cracking is much higher than that of fiber rupture as indicated in the bottom right plot. The twist angle is adjusted so that Hashin's failure criteria [4] indicate near exhaust of matrix strength.

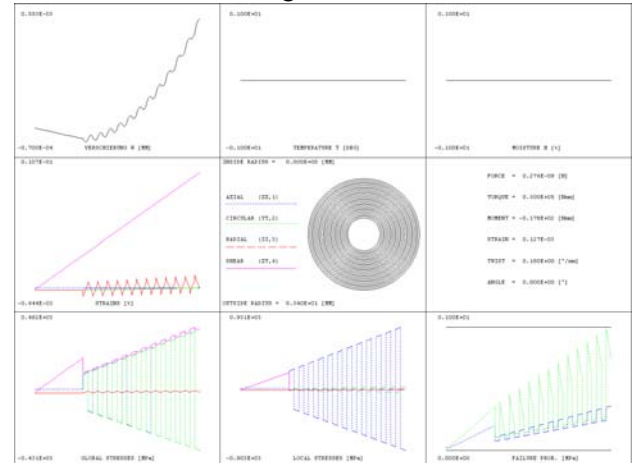


Fig. 2. Graphical Output Window TUBE program

The deformation energy u per unit length is calculated by multiplying the applied limit torque T with the obtained twist angle ϕ . How these depend on the relative mandrel radius $\rho = R_M/R_S$ is shown in Fig. 3. T increases with increasing mandrel radius up to $\rho \approx 0.7$ where ϕ remains relatively constant. Within this range, the structural strength is limited by matrix failure in the composite material. Beyond it the steel fails first so that the limit torque curve goes through a local minimum at $\rho \approx 0.8$. The following increase is because of the shear modulus of the steel being much higher than that of the composite material.

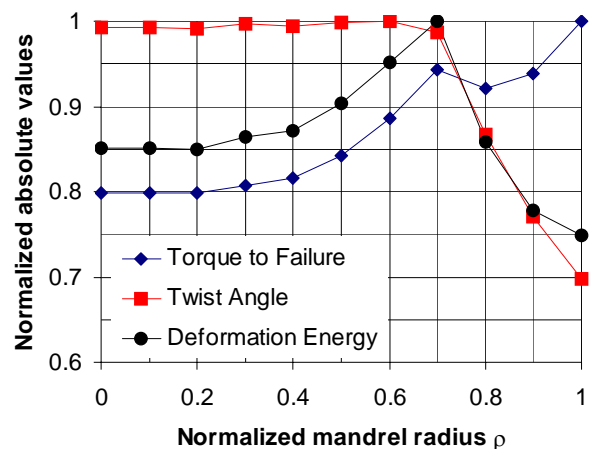


Fig. 3 Spring efficiency

A pure composite spring can store more deformation energy than one of steel but the material combination of a steel mandrel within a composite body obtains even higher efficiency, for the here estimated material properties, when $r \approx 0.7$. The mass-specific spring energy, shown in Fig. 4, is highest if the spring consists of composite material only and decreases with increasing mandrel diameter. The specific properties are relevant for all lightweight objectives such as low unsprung mass.

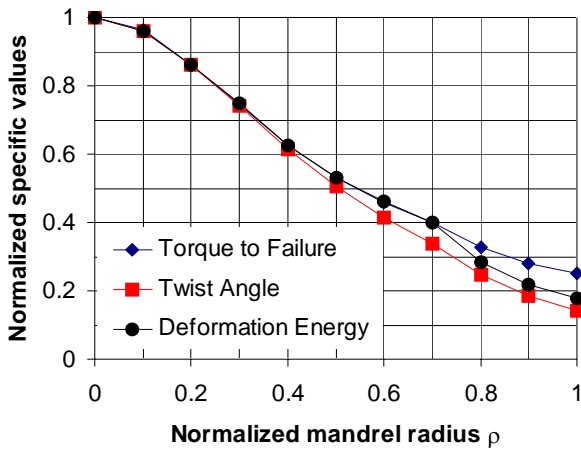


Fig. 4. Mass-specific spring efficiency

3 Load Introduction Problems

The most obvious question is how to introduce the torque into a CFRP bar and we propose a hypothetical answer to it by the design principle indicated with Fig. 5.

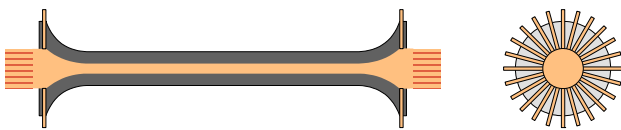


Fig. 5. Fiber-wound torsion bar design principle

The CFRP torsion bar is fiber wound by using a mandrel with enhanced functionality: its diameter increases at the ends and there an annulus of spikes holds the fiber strands in place at the fiber-path turns. Beyond the spike annulus there is a region which can be serrated for connecting other parts with the torsion bar. The diameter increase reduces the stresses holding equilibrium to the applied torque.

4 Design and Analysis models

4.1 Geometry Model

Fig. 3 uses a plot produced by the program to explain the geometry modeling. The numbers indicate the following measures:

- (1) active length of torsion bar
- (2) length of load introduction zone
- (3) width of side disk
- (4) width of groove toothing
- (5) base mandrel radius
- (6) active spring radius

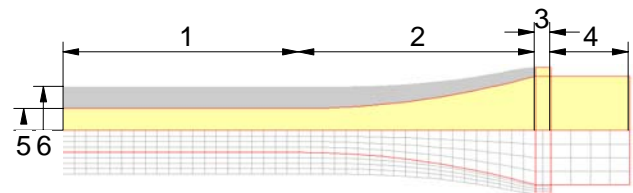


Fig. 6. Geometry Model

Other measures, not shown in the Figure, are obtained by the fibre winding simulation and the automatic optimization procedure explained in Section 5.

4.2 Fiber Winding Simulation

The mandrel geometry is divided into two sections: the active spring zone $0 \leq y \leq y_1$ with constant mandrel base radius r_{mb} , and the load introduction zone $y_1 \leq y \leq y_2$ where the radius $r(y)$ tends to increase towards y_2 . The fibre winding process leads to interwoven fibre architecture but, simplifying, we assume a laminate structure with distinguishable unidirectional layers. The most efficient fibre orientation for torsion is $\varphi = \pm 45^\circ$.

Geodetic fibre winding obeys Clairaut's law

$$r \sin(\varphi) = c = const \quad (5)$$

and implies that the angle φ decreases with increasing mandrel diameter. When fiber angles deviate from the optimum $\varphi = \pm 45^\circ$, both stiffness and strength of the fiber-wound body decrease. It

interests us how the negative effect of fiber angle decrease and the positive effect of diameter increase combine with regard to the load introduction problem. For an absolute fiber angle $\varphi = \pm 45^\circ$ in the active spring zone, we find, before placing the first layer, for the constant in Eq. 5

$$c = r_{mb} \frac{\sqrt{2}}{2} \quad (6)$$

A change of radius, from r_{mb} to $r_m(y)$, then changes the absolute value of the fiber angle so that

$$\varphi(y) = \frac{\arcsin(c)}{r_m(y)} \quad (7)$$

A layer thickness h_a within the active-spring section changes by the geometric mechanism illustrated in Fig. 7. The sketch on the left-hand side of the figure depicts the geometry at a reference radius r_0 and the other one captures the effects of changing the radius from r_0 to r .

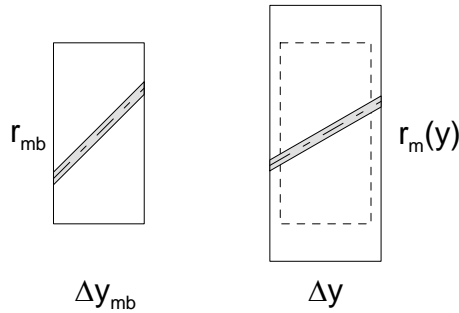


Fig. 7. Mandrel Diameter Influence on Thickness

The shaded regions represent a fiber strand of unit length at different angles and both regions contain the same volume. The axial length increment Δy follows from

$$\Delta y = \cos(\varphi(y)) \quad (8)$$

The area over which the volume of the unit length fiber strand must be distributed changes from $A_0 = r_0 \Delta y_0$ to $A(r) = r \Delta y(r)$. Consequently, a layer thickness $h(r)$ refers to a reference value h_a , specified for the active spring region, by

$$h(y) = h_a \frac{r_{mb} \Delta y_{mb}}{r \Delta y} = h_a \frac{\sqrt{2} r_{mb}}{2r \cos(\varphi(y))} \quad (9)$$

Because of

$$\cos = \sqrt{1 - \sin^2}, \quad \sin(\varphi) = \frac{c}{r} \quad (10)$$

we find that

$$h(r) = h_a \frac{\sqrt{2} r_{mb}}{\sqrt{r^2 - c^2}} = h_a \frac{r_{mb}}{\sqrt{2r_m^2 - r_{mb}^2}} \quad (11)$$

The above formulae assume the specified layer thickness h_a be small if compared with the mandrel base radius r_{mb} , or $h_a \ll r_{mb}$. If the assumption holds not true, one must subdivide the layer thickness into a sufficient number n of sub-layers and evaluate the recursion

$$h(y) = \sum_{k=1}^n h_k(y) = \sum_{k=1}^n \frac{h_a}{n} \frac{r_{mb} + \frac{k}{n} h_a}{\sqrt{2 \left(r_m(y) + \sum_{l=1}^{k-1} h_l(y) \right)^2 - \left(r_{mb} + \frac{k}{n} h_a \right)^2}} \quad (12)$$

If the radius changes quickly along the axis, the thickness increment, which adds perpendicularly to the surface, must be decomposed in the r and y directions. It must also be taken into account that each layer produces a new surface which acts as a mandrel for the following layer. Finally, modeling of the structural behavior of the fiber-wound body requires transformation of the material law. There are two directions about which transformation must be performed: first about the radial direction r for the winding angle φ and then about the circumferential direction θ for the angle $\beta = \arctan(r(y))$.

A pure ± 45 fiber architecture, extending from the active spring region to the end of the load-introduction zone, promises optimum efficiency but can only be achieved if slippage of the fibers during a non-geodetic fiber winding process can be prevented. The change of thickness with radius is then described with

$$h(r) = h_0 \frac{r_0}{r} \quad (13)$$

4.3 Analysis Model

We consider a state of rotational symmetry and use the reference coordinates y , θ , and r for the axial, circumferential, and radial directions, respectively. Because of the anisotropy of the CFRP material we start with the general kinematical equations in cylindrical coordinates which we simplify by ignoring the circumferential variations of the strains and stresses:

$$\begin{aligned}
 \varepsilon_y &= u_{y,y} \\
 \varepsilon_\theta &= \frac{u_r}{r} \\
 \varepsilon_r &= u_{r,r} \\
 \gamma_{\theta r} &= u_{\theta,r} - \frac{u_\theta}{r} \\
 \gamma_{\theta y} &= u_{r,y} + u_{y,r} \\
 \gamma_{y\theta} &= u_{\theta,y}
 \end{aligned} \tag{14}$$

The equilibrium conditions are:

$$\begin{aligned}
 \sigma_{y,y} + \frac{(r\tau_{ry})_{,r}}{r} &= 0 \\
 \frac{(r^2\tau_{\theta r})_{,r}}{r} + \tau_{ry,y} &= 0 \\
 \sigma_{r,r} + \frac{(\sigma_r - \sigma_\theta)}{r} + \tau_{y\theta,y} &= 0
 \end{aligned} \tag{15}$$

The stresses and strains are connected by the material law

$$\mathbf{C} = \begin{bmatrix} c_{11} & c_{12} & c_{13} & 0 & 0 & c_{16} \\ c_{12} & c_{22} & c_{23} & 0 & 0 & c_{26} \\ c_{13} & c_{23} & c_{33} & 0 & 0 & c_{36} \\ 0 & 0 & 0 & c_{44} & c_{45} & 0 \\ 0 & 0 & 0 & c_{45} & c_{55} & 0 \\ c_{16} & c_{26} & c_{36} & 0 & 0 & c_{66} \end{bmatrix} \tag{16}$$

The finite-element method (FEM) [5] finds the numerical system equations for the nodal point displacements

$$\mathbf{K}\tilde{\mathbf{u}} = \mathbf{r} \tag{17}$$

The system stiffness matrix \mathbf{K} is assembled from the element contributions

$$\mathbf{K} = 2\pi \sum_1^{N_{EL}} \int_{\Omega_{EL}} \mathbf{B}^T \mathbf{C} \mathbf{B} r dr dy \tag{18}$$

and the specified natural boundary conditions $\hat{\sigma}$ give the nodal-point forces

$$\mathbf{r} = 2\pi \sum_1^{N_{EL}} \int_{\Gamma_{EL}} \Phi r \hat{\sigma} ds \tag{19}$$

The symbol \mathbf{B} relates the element strains to the nodal point displacements and J stands for the determinant of the Jacobian matrix. Fig. 6 indicates that a geometric symmetry with respect to the center cross-section exists. Strain and stress distributions find the same symmetry which is therefore exploited to enhance numerical efficiency. At the center cross-section geometric boundary conditions prevent axial and circumferential displacements. External torque is applied at the end where a tooth grooving is thought to exist even though not modeled in detail. There, Eq. 19 transforms an externally applied constant circumferential stress distribution $\hat{\sigma}$ into kinematically equivalent nodal forces \mathbf{r} .

5 Optimization Model

A torsion bar can not at the same time be arbitrarily compliant, bearing very high torque, and small. We have therefore chosen to design the torsion bar in two steps. The first step is to choose a design for the active length of the torsion bar where the mandrel and fiber-wound body are constant along the longitudinal direction. The second step is to find a design for the load introduction zone so that it can transmit the torque into the active length without creating peak stresses or wasting material. It is here where we apply automated optimization.

5.1 Objectives and Constraints

The objective of maximum energy storage capacity U implies that the active length is stressed to the limit before failure in the load introduction zone occurs. It also implies that the load introduction zone itself is as compliant as possible, adding to the overall spring efficiency. Apparently, the compliance is constrained by strength: the specified torque must cause neither the mandrel nor the fiber-wound body to fail.

Thus, we state the constrained optimization problem as

$$\min_{x \in R^n} \{-U(x) | g(x) \leq 0\} \quad (20)$$

The vector of constraining functions g contains the two entries $g_{mandrel}$ and g_{cfRP} . We assume that the mandrel consists of an isotropic material, where steel is a likely candidate. Then the strength can be checked by comparing an equivalent stress σ_{eqv} with an admissible stress σ_{adm} ,

$$g_{mandrel} = \sigma_{eqv} - \sigma_{adm} \leq 0 \quad (21)$$

using either Tresca's [6] maximum principal stress criterion or the von Mises [7] distortion energy hypotheses or, to be on the safe side, both. There are a number of failure criteria for unidirectional CFRP with different prediction abilities. Those by Tsai and Hill [8] or Tsai and Wu [9], for instance, use composite strength values and the stress state to evaluate an index a value of which in excess of one indicates failure, without any indication regarding the nature of it. Such criteria are, however, more conservative than the maximum stress criterion which distinguishes between fiber and matrix failure but does not take into account interaction between the various stress components. Better suited are the criteria by Hashin [4]: they predict fiber and matrix failure separately and take into account the effects of tensile and compressive stressing, which makes a set of four different criteria. Puck provides a physically better founded hypothesis [10] for matrix failure which provides the practitioner with the opportunity to obtain predictions better aligned with reality if he succeeds in procuring the necessary additional strength parameters. Here we choose Hashin's criteria which inform us that the strength limits of the fiber-wound body are defined by matrix failure.

The constraining function then becomes

$$g_{cfRP} = \max(f_1, f_2, f_3, f_4) - 1 \leq 0 \quad (22)$$

where the f_i stand for Hashin's four individual fail-ure criteria. The exterior penalty method transforms the problem statement Eq. 20 so that the minimum of a pseudo-objective function may admit only slight constraint violations

$$\min_{x \in R^n} \{P(x)\} \quad (23)$$

if the penalty factor R_p is set high enough

$$P = -U + R_p(\Omega_{mandrel} + \Omega_{CFRP}) \quad (24)$$

The penalty functions Ω_i are calculated with

$$\Omega_i = \{\max[g_i(\mathbf{x}), 0]^2\} \quad (25)$$

5.2 Optimization Variables

The variable design feature is the radius distribution of the mandrel within the load introduction zone including the side disk and the groove toothing. We invent free parameters only for the mandrel. The side disk radius equals the total radius of the adjacent fiber-wound body and the groove toothing radius is the same as that of the mandrel at the other side of the side disk. The thickness of the mandrel we parameterize with polynomial functions which should be even with respect to the center cross-section:

$$r_m(y) = r_a + x_1\eta^2 + x_2\eta^4 + x_3\eta^6 \quad (26)$$

where the normalized coordinate η is convenient

$$\eta = \frac{y - y_1}{y_2 - y_1} \quad (27)$$

Here, y_1 and $y_2 - y_1$ are the lengths of the active spring region and the load introduction zone, respectively.

5.3 Design Improvement

Starting from a given initial design the method of conjugate gradients [11] seeks improved solutions by minimizing the pseudo-objective Eq. 24. The method determines search directions \mathbf{s} along which best solutions must be identified by a line search. For the line search we use the method called Brent's routine [12] which combines the golden-section and quadratic-approximation methods. In contrast to the maximum-compliance objective, the strength constraints are not convex because the locations at which maximum stressing occurs may switch when changing the design variables. It is therefore that the here selected method of mathematical programming must be applied with care and finding the best design solution may depend on the choice of the starting point in variables space.

6 Results

The fixed design parameters include a length of $l = 1000mm$ and a diameter $d = 20mm$ of the fiber-wound body and we apply a torque $T = 1000Nm$. These data allow reference to the preliminary results presented in Section 2.2. It is only for the benefit of the better visualization of the load transfer mechanism that we use for it the smaller length of $l = 100mm$.

6.1 Load Transfer Mechanism

The upper half of each plot shown in Fig. 8 visualizes the distribution of the circumferential displacement u_μ where darker shades of grey correspond with higher displacement values. They increase with increasing distance from both the center cross-section and the axis of rotation, reaching maximum values at the side disk edge.

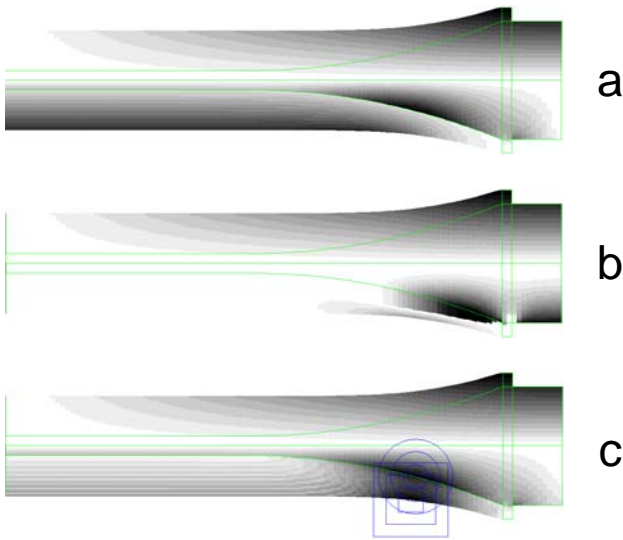


Fig. 8. Torsion Bar Load Response

The lower halves of the plots visualize the distribution of stresses $\tau_{y\theta}$ (a), $\tau_{\theta r}$ (b), and the failure indices (c) in the mandrel and fiber-wound body.

The torsion shear stress distribution $\tau_{y\theta}$ (a) provides, together with the material compliance, the spring energy. It also tends to increase with increasing distance from the axis of rotation and the increase is fastest within the steel mandrel and the load introduction zone. This effect and the jump at the interface between the mandrel and fiber-wound

body have a common cause: the shear stiffness of steel is higher than that of the composite. Noting the similarity between the distributions plotted in (a) and in (c) lets suspect that the torsion shear stress contributes most to the failure probability of the materials.

The elements where the highest failure index values appear are marked in (c) with circles (mandrel) and squares (composite). One can also see that the failure index values in the active spring-region globally increase with radius but vary from layer to layer because the fibers are alternatively loaded in tension and compression, respectively.

The shown design solution can not be optimum since failure will occur within the load-introduction zone before the fiber-wound body can store a maximum of deformation energy. However, the low values of failure indices adjacent to the side disk answer our key question, of whether the proposed design principle is feasible, in the affirmative.

The mechanism of load transfer from the tooth-grooved end through the mandrel into the fiber-wound body evokes the shear stress $\tau_{\theta r}$. To better visualize the mechanism, the plot (b) has been scaled with respect to the highest value appearing between center cross-section and side disk.

6.2 Active-Spring Length Fraction Influence

We investigate the influence of the length of the active spring region on the torsion spring performance and for it we keep the base mandrel diameter at $d = 1mm$. Fig. 9 shows torsion angle, mass, and the failure indices for mandrel and fiber-wound body for the various length ratios of active spring to fiber-wound body.

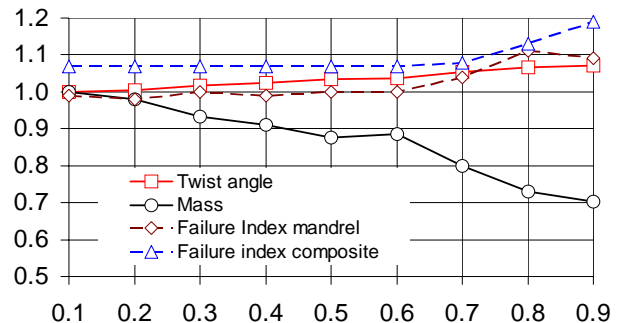


Fig. 9. Influence of Active-Spring Length Fraction

With increasing length ratio the torsion angle increases monotonically but the monotony of mass decrease is interrupted at $l_{as}/l = 0.6$. The

composite-failure index stays initially constant at $i_c = 1.07$ and starts to increase at $l_{as}/l = 0.7$. Both effects have to do with the shifting of the location where the composite strength first reaches its limit: initially the critical point lies within the active-spring region and then it moves into the load-introduction zone.

This implies that, in practice, length ratios should be kept small enough for the critical stressing of the composite to remain in the active-spring region or, with the present data set, $l_{as}/l \leq 0.5$.

6.3 Mandrel Base Diameter Influence

Here we investigate the influence of the mandrel base diameter and for it we keep the active spring length ratio $l_{as}/l = 0.1$. Since the torque is always $T = 1000 Nm$ and the steel material provides higher shear modulus than the composite, the twist angle decreases with increasing mandrel base diameter as Fig. 10 shows.

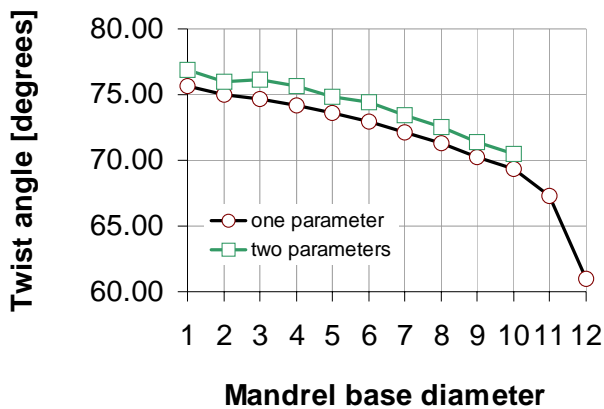


Fig. 6. Twist Angle

The lower curve corresponds with using, in polynomial shape parameterization (26), only x_1 and the upper one is achieved using x_2 also. Including the third parameter x_3 did not give noticeable further change of results.

Obviously, larger values of the mandrel base diameter incur further disadvantage in terms of weight increase as Fig. 11 testifies.

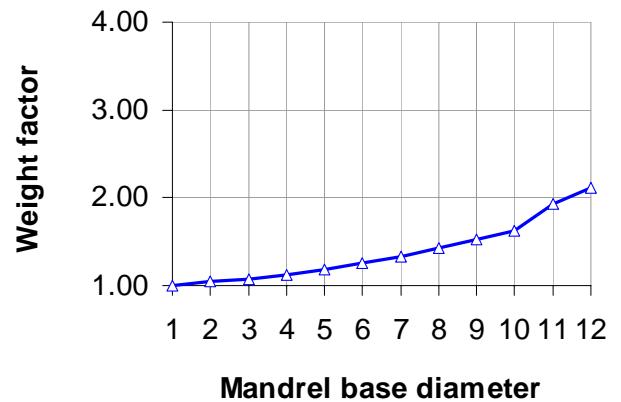


Fig. 11. Weight Factor

We have noticed in Section 4.1 that the load transfer mechanism relies mostly on the shear component $\tau_{y\theta}$ and Fig. 8 shows the distributions along the interface between mandrel and fiber-wound body for the different values of mandrel base radius. It appears that absolute stress values tend to increase with decreasing d_{base} but at $d_{base} \approx 10mm$ a change-of-sign occurs. Since this boldly plotted stress curve exhibits the lowest absolute stress values, the said diameter value holds the lowest risk of losing interface contact which plays such a crucial role in the load transfer mechanism.

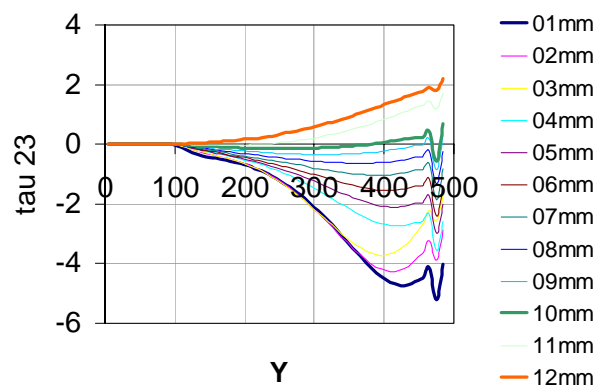


Fig. 8. Shear Stress $\tau_{y\theta}$ Distribution

Conclusions

Even though early matrix cracking prevents the full utilization of fiber strength, torsion bars made from CFRP can store higher deformation energy than those made from steel. The advantage increases if one is interested in lightweight design solutions.

The search for an answer to the question of how to introduce the load into the composite bar has led to a design principle where a CFRP body is wound around a multi-functional steel mandrel which increases its radius towards the end which holds a spike annulus and also serves as adapter to connect with external parts.

The shape transition from the active-spring to the load-introduction zones has been optimized by using a parameterized geometry model and a mathematical programming technique. The geometry model takes, via fiber winding simulation, into account the dependence between mandrel and CFRP body shapes. The FEM analysis model utilizes rotational symmetry but calculates a fully three-dimensional stress state.

The identified design problem is to reach an almost even distribution of failure probability along the bar and for both materials.

The further problem of interface failure between mandrel and CFRP has also been addressed. It has been shown that the base mandrel diameter can be adjusted to minimize the interface shear stress $\tau_{y\theta}$.

References

- [1] Sass, F. Bouché, Ch., and Leitner, A. *Dubbel: Taschenbuch für den Maschinenbau*. Springer, 1974
- [2] Jones, R.M. *Mechanics of composite materials*. Taylor & Francis, Inc., Philadelphia, 1999
- [3] Kress, G. Minimized computational effort for the thick-walled composite tube problem. *Computers and Structures*, Vol. 54, No. 4, pp 633-639, 1995
- [4] Hashin, Z. Failure criteria for unidirectional fiber composites, *Journal of Composite Materials*, Vol. 7, pp 329-334, 1980
- [5] Reddy, J.N. *An introduction to the finite-element method*. McGraw-Hill, Inc., 1985
- [6] Tresca, H. Memoire sur lecoulement des corps solides soumis a de fortes pressions. *Comptes Rendus*, Vol. 59, pp 754, 1864
- [7] Von Mises, R. Mechanik der plastischen Formänderung von Kristallen. *Zeitschrift für Angewandte Mathematik (ZAMM)*, Vol. 8, No. 3, pp 161-195, 1928
- [8] Tsai, S.W. *Fundamental aspects of fiber reinforced plastic composites*. Wiley Interscience, 1985
- [9] Tsai, S.W. and Wu, E.M. A general theory of strength for anisotropic materials. *Journal of Composite Materials*, pp 58-80, 1971
- [10] Puck, A. *Festigkeitsanalyse von Faser-Matrix-Laminaten*. Hanser, Munich, Wien, 1996
- [11] Fletcher, R. and Reeves, C.M., Function minimization by conjugate gradients. *Computers Journal*, Vol 7, No. 5, pp. 149-154, 1964
- [12] Brent, R.P. *Algorithms for minimization without derivatives*. Prentice Hall, Englewood Cliffs, NJ, 1973